Silent marine operations with Azipod® propulsion

J Roivainen* D.Sc., T Sipilä Lic. Sc.

ABB Marine and ports, FI
* Corresponding Author. Email: janne.roivainen@fi.abb.com

Synopsis

Azipod® propulsion is a gearless steerable propulsion system where the electric drive motor is located outside the ship hull in the pod housing. The shaft is directly connected to the electric motor driving the propeller. The Azipod ® propulsion units can be steered 360 degrees using a steering system located inside the ship hull. Due to this arrangement, the electric drive motor becomes a significant underwater noise source as it is located outside the ship hull. Propeller hydrodynamic noise is another important noise source in propulsion. Especially, when exceeding the cavitation inception speed, hydrodynamic noise becomes equally or even more important underwater radiated noise (URN) source as the electromagnetic noise. The inflow to the propeller is smooth in pulling Azipod ® propulsion helping to control cavitation and to delay the inception speed. This paper discusses noise measurement-, prediction- and mitigation methods for electric motor emitted URN (MURN) and propeller emitted URN (PURN).

Keywords: Azipod®; Magnetic noise; Propeller noise; Propulsion; Marine systems

1. Introduction

Acoustically the submerged components of an Azipod® propulsion unit comprise two uncorrelated noise sources, namely the propeller and the electrical motor. The propeller hydrodynamic noise is highly dependent on the load & speed whereas the magnetic noise is much less dependent of the loading.

The propeller induced underwater noise (PURN) compounds of thickness and loading noise, turbulence noise, and cavitation noise. The sources of thickness and loading noise are dipole type, which means that they do not radiate to far-field efficiently. The thickness and loading noise are very important to contributors to the pressure excitations to the ship bottom at tonal of blade passing frequency and its harmonics and are important from the inboard comfort point of view. Turbulence noise can be divided into two categories. Leading edge turbulence noise is low frequency broadband noise which is triggered when the blade penetrates the boundary layer of ship hull. High frequency broadband turbulence noise is caused by the turbulent boundary layer of the blade itself due to the vortex shedding at the trailing edge. An inception is a case where the vortex shedding at the trailing edge awakes the eigenmodes of the blade causing an intense discrete peak to the noise spectrum, which is also known as propeller singing.

Cavitation noise is dominating vessels' noise spectrum after inception speed and contributes to noise spectrum from blade passing frequency (about 10 Hz) to 20 000 Hz and above. Sheet cavitation increases tonal noise at blade passing frequency and its harmonics. The most relevant cavitation types for broad band noise are bubble cavitation and vortex cavitation. Tip vortex cavitation has contribution on tonal noise and especially to broadband noise. Cavitation is of monopole type noise source so that it propagates efficiently to far field in the underwater environment. Practically all merchant ships have transit speed above cavitation inception speed. For that, cavitation noise is very important contributor in underwater sound field in oceans.

The electromagnetic noise of the motor (MURN) is highly dependent on the converter supply properties such as the drive nominal voltage (Medium- or Low voltage), number of voltage levels and current/voltage modulation parameters, which is true for all types of electrical motors: induction-, synchronous-, reluctance and permanent magnet motors. Another factor affecting the electromagnetic noise emission lies in the motor design itself: slot numbers, magnetic pole shaping, magnetic slot wedges, stator winding properties, magnetic saturation of iron etc. Thus, the electromagnetic noise is made up from two components: converter- and self-noise.

The MURN process includes three physical mechanisms: 1) Magnetic forces exciting the structure, 2) Structural deflections or vibration due to excitations and 3) Sound radiation due to structure-fluid interface vibration. The MURN mitigation actions usually concentrate on reducing the system excitation energy, i.e., minimization of the magnetic forces.

Authors' Biography

Janne Roivainen was born in 1967. He received the M.Sc. degree in technology and the D.Sc. degree in technology from Helsinki University of Technology, Espoo, Finland, in 1994 and 2009, respectively. He worked for ABB Motors and Generators, Helsinki from 1994 to 2022 dealing with testing and noise & vibration issues related to electric machines. Currently he is working for ABB Marine with focus on underwater noise. He is convenor for IEC TC2/MT2 and member of CIMAC WG22 (underwater noise).

Tuomas Sipilä was born in 1978. He received the M.Sc. degree in technology and the Lic. Sc. degree in technology from Helsinki University of technology, Espoo, Finland in 2004 and 2014, respectively. He worked at VTT technical research center of Finland in hydrodynamics and underwater noise 2004-2020, and leading the Ship and arctic technology team in 2015-2020. Currently he is working at ABB Marine and Ports focusing on hydrodynamics and underwater noise. He was a member of 28th and 29th ITTC specialist committee on hydrodynamic noise in 2014-2017 and 2017-2020.

Once the objectives are set and actions taken to mitigate propulsor URN, there must be a way to monitor the outcome. One option is to arrange a standard far-field measurement session to validate the mitigation results. As the far-field measurements are costly, they are carried out only once in stationary conditions. The onboard measurement approach provides an alternative, being able to track URN continuously and provide insight also to off-design conditions.

2. Propeller emitted URN (PURN)

Tip vortex cavitation is the dominant noise source in vessels where cavitation where sheet cavitation has been suppressed in propeller design phase. The volume fluctuations in the tip vortex cause a broadband hump at the noise spectrum around about 100 Hz frequency, depending on the main dimensions and power of the propeller. Azipod® units are typically installed to vessels where the hull lines give smooth wake field to the propeller and propeller tip vortex cavitation is the dominant hydrodynamic noise source.

2.1. Dynamics of vortex cavitation

Tip vortices form behind lifting surfaces, such as propeller blade, due to the pressure difference between the pressure and suction side of the lifting surfaces. At the tips of the lifting surface, the pressure difference forces the flow to rotate from the pressure side to the suction side.

Tip vortex generation can be explained following the potential flow theory. Kelvin's theorem states that circulation Γ around any closed material curve is constant in time:

$$\Gamma = \oint_{\gamma(t)} \vec{v} \cdot d\vec{l} \tag{1}$$

where $\gamma(t)$ is vorticity, and $\vec{v}$ is velocity vector and $d\vec{l}$ is a length element in a curvilinear path $\vec{l}$. Circulation can also be expressed as a spread vorticity $\vec{\zeta}$ on a material surface S as $\Gamma = \iint_S \vec{\zeta} \cdot \vec{n} dS$, where $\vec{n}$ is unit normal vector. The vorticity is defined as

$$\vec{\zeta} = \nabla \times \vec{v}. \tag{2}$$

As the circulation is constant, also the vorticity flux must be constant. The Helmholtz theorem states that a vortex line is a material line. The same holds also for a vortex sheet, which is a surface comprising all vortex lines passing through a closed curve $\gamma(t)$.

Vorticity can be divided into bound and free vorticity. The bound vorticity carries the load on the foil whereas the free vorticity locates in the slipstream of the foil and is responsible for the induced drag of the flow field. Figure 1 shows an elliptical lifting surface and the related bound and free vorticity field. The roll-up process of the free vorticity field into tip vortices is also illustrated in the figure. The roll-up process is driven by the self-induced velocities of the free vortices in the slip stream. The circulation in the tip vortices is progressively increased in the slip stream as the roll-up process develops. Far downstream from the hydrofoil the circulation in the tip vortices reaches its maximum $\Gamma = \Gamma_{max}$, where Γ_{max} is the maximum spanwise circulation on the lifting surface.

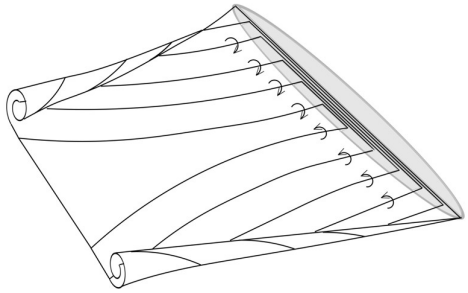

Figure 1. Roll-up of free vorticity field at the slipstream of a lifting surface.

The tangential velocity inside a two-dimensional potential flow vortex is calculated as:

$$v_\theta(r) = \frac{\Gamma}{2\pi r}. \tag{3}$$

This formulation gives unrealistic high velocities in the vortex core where vorticity and viscosity have a significant role, and potential flow theory does not apply anymore. The simplest viscous vortex model is presented by Rankine (1869). In Rankine model the core of the vortex is modelled as a solid disk. The tangential velocity inside the rotational core is determined as

$$v_\theta(r) = \frac{\Gamma}{2\pi a^2} r \tag{4}$$

where a is the radius of the rotational vortex core. Outside the rotational core, the velocities induced by the vortex are calculated using Eq. 3. The tangential velocity has its maximum at $r = a$.

Another famous vortex model is the one from Burgers (1948). This model considers the diffusion of vorticity in the fluid and the stretching of the vortex. The tangential velocity induced by the Burgers vortex model is:

$$v_\theta(r) = \frac{\Gamma}{2\pi}\left(1 - e^{-\beta\left(\frac{r}{a}\right)^2}\right) \tag{5}$$

where $\beta = \frac{\gamma}{4\nu}$. The stretching γ can be a constant or a variable. The viscous core radius is calculated as $a = \sqrt{4\nu t}$.

The pressure distribution induced by the vortex can be determined utilizing Bernoulli equation for the irrotational part of the flow field and Euler equations for the rotational core of the vortex. The derivation of pressure in the vortex core is presented in hydrodynamics textbooks. In the potential flow part of the vortex, the pressure is determined as:

$$p = p_\infty - \frac{\rho}{2}\frac{\Gamma^2}{4\pi^2 r^2} \tag{6}$$

Rankine vortex model predicts the pressure in the vortex core as:

$$p = p_\infty + \frac{\rho}{2}\left(\frac{\Gamma}{2\pi a}\right)^2\left[\left(\frac{r}{a}\right)^2 - 2\right] \tag{7}$$

and the Burgers vortex model as

$$p - p_\infty = -\rho\left(\frac{\Gamma}{2\pi}\right)^2 \int_x^\infty \frac{\left(1-e^{-\beta\left(\frac{r}{a}\right)^2}\right)^2}{\left(\frac{r}{a}\right)^3}\mathrm{d}r \tag{8}$$

Figure 2 shows the velocity and pressure distribution of different vortex models. It is seen that the velocity and pressure distributions are less pronounced in the Burges vortex model. The Burgers vortex model joins the results of potential flow vortex at about $r/a = 2.0$.

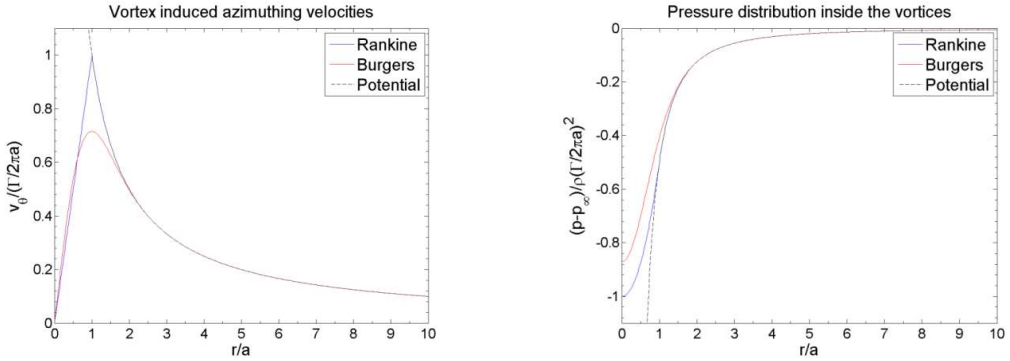

Figure 2. Tangential velocities (left) and pressure distribution (right) as described by potential flow, Rankine, and Burgers vortex models.

Cavitation affects the vortex core significantly, as the pressure inside the vortex cannot fall below vapor pressure. Cavitating tip vortices are subject to changes in length and ambient pressure. If the ambient pressure is kept constant, vortex stretching increases the rotational velocity of the vortex. This increases the size of the cavitating core of the vortex. In case the vortex length is constant, and the ambient pressure varies, a twofold phenomenon develops. Increase in ambient pressure decreases the size of the vortex. This consequently increases the rate of rotation which, in turn, increases the size of the cavitating core of the vortex. The latter secondary effect raises the natural oscillations of the isolated vortices (Franc and Michel, 2004).

2.1.1. Noise model of vortex cavitation

ABB uses ETV (empirical tip vortex) method to estimate underwater noise from propellers. Tip vortex cavitation is the dominant source in propeller designs in ships that are equipped with Azipod® propulsors. The ETV model is developed in CRS (Co-operation Research Ships) and is described in detail in Bosschers (2018). The method is calibrated by full scale measurement data.

In the ETV model, vortex strength is calculated with a selected vortex model. The cavitating vortex core radius is determined based on the outcome of the vortex model. The cavity radius is used to estimate the source level spectrum from cavitating tip vortex. The resonance frequency of the vortex f_c is determined based on the theoretical considerations with empirical tuning factors as

$$\frac{f_c}{f_{bpf}} = \tau \frac{D\sqrt{\sigma_n}}{r_c Z} \tag{9}$$

where f_{bpf} is the blade pass frequence, σ_n is the cavitation number, Z is the blade number, D is the propeller diameter, and τ is calibration factor. The maximum of the hump of the broadband spectrum is determined as

$$L_{p,max} = a_p + 20\log_{10}[\left(\frac{\tau r_c}{D}\right)^{k_p}\sqrt{Z} \tag{10}$$

where a_p and k_p are empirical factors. The slopes at both sides of the maximum of the spectrum are determined empirically. Figure 3 shows an example of simulated noise using ETV for a cruise liner together with far field noise measurements. The simulated magnetic noise from the electric motor is also shown in the figure. Good correlation is seen between the ETV noise predictions and the full-scale measurements.

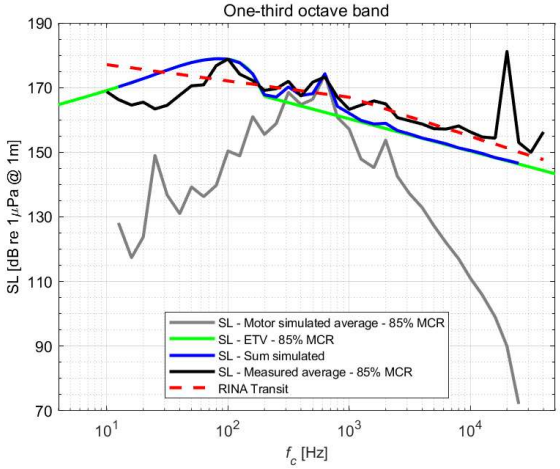

Figure 3. Comparison of predicted URN source level using ETV-model to far-field noise measurements from a vessel without noise restrictions. Magnetic noise from propulsion motor is also shown. Rina transit limit is given for reference.

2.2. PURN mitigation

As discussed above, propeller tip vortex is the dominant noise source in many propeller designs. The strength of the tip vortices can be reduced by unloading the tip of the propeller blades. Unfortunately, that will lead to a decrease in propulsion efficiency.

A good compromise between noise and efficiency can be achieved when a careful wake adapted propeller design is performed where the inflow characteristics are considered. Propeller is a complex three-dimensional geometry where the propeller diameter, blade area ratio, pitch, thickness, camber, chord, skew, and rake distributions, and section profile geometry needs carefully adjusted for the ship specific needs to give desired performance and excitation levels.

It is a large effort to optimize all these parameters by hand. Therefore, ABB uses an optimization library PropArt, developed in CRS, to find the best options for propeller designs. The optimization routine creates several individual designs for several optimization generations where the convergence of the solution can be followed. The optimization looks for the optimum propeller design based on the goals and constraints that the user has given as input.

The optimization algorithm compares the goals and constraints with respect to the analysis of each individual propeller design. As the optimization is converging, a pareto front is formed from the individual designs showing the trade-off of conflicting objectives. An example of a pareto front is shown in Figure 4 where the optimization results are given for propeller efficiency and ETV noise index. Pareto front shows what is the trade-off in optimized designs between different goals.

The propeller designer must carefully investigate and fine-tune the design that PropArt optimization delivers. Detailed CFD analyses are usually done to the final design propeller before delivering the geometry to model tests. The optimization done with PropArt helps to find the correct parameters to the propeller design with less manual effort compared to a case where the whole process is made by the propeller designer him/herself.

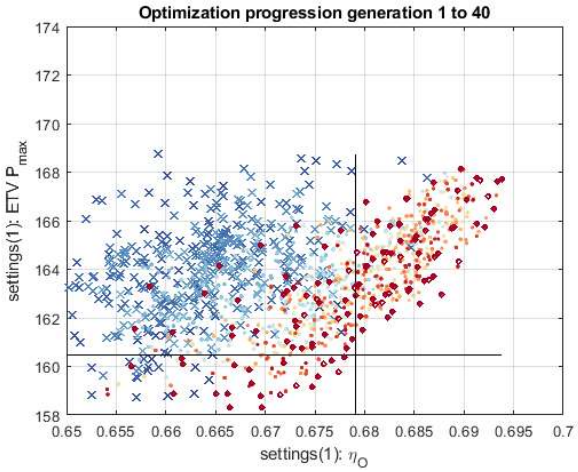

Figure 4. Convergence of propeller optimization. Each point represents a propeller design variant. A pareto front is clearly developed in efficiency (η_O) and noise index (ETV)

3. Electric motor emitted URN (MURN)

MURN is originated in the electric motor between stator and rotor, where the time varying magnetic field tries to close the airgap between them. The magnetic force or traction generation mechanisms are non-linear meaning that a supply voltage with frequency f_1 creates a spectrum of traction components. Figure 5: left shows the total radial traction for an induction motor supplied with sinusoidal voltage at 4.5 MW load, f_1=15 Hz.

3.1. Magnetic traction

The magnetic field solution at a given loading and speed is nowadays calculated with non-linear 2D FE-solver in time domain. As the numerical magnetic field solution does not provide physical insight to the magnetic force generation itself, a classical rotating-field theory is used in the following text (Timar, 1989). In fact, the numerical magnetic field solution is also transformed by 2D FFT into rotating waves. Figure 5: right shows a cross section of a typical induction motor. In the derivation of rotating waves, all the magnetic flux is assumed to penetrate the stator teeth through their tips.

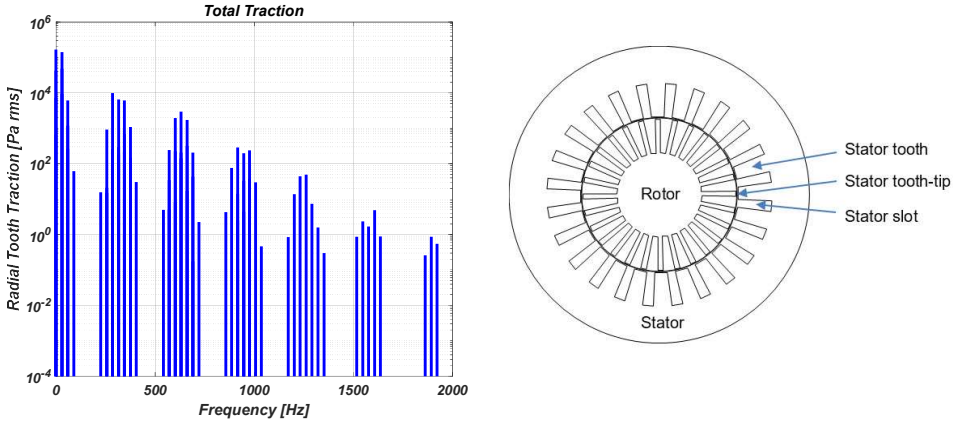

Figure 5: Left: Total radial traction with sinusoidal voltage, right: Cross-section of an induction motor

Once the motor is energized, the voltage component at supply frequency generates a fundamental rotating magnetic wave field with flux density B_1 expressed in cylindrical coordinates:

$$B_1 = k_1 U e^{j(p\varphi - \omega_1 t + \alpha_1)} \tag{11}$$

, where k_1 is arbitrary constant, U the supply voltage, p is the pole pair number of the motor, φ is circumferential cylindrical coordinate, ω_1 is supply frequency, t is time and α_1 is an arbitrary phase angle. The fundamental component is the only one needed to create the desired power and torque. Since the motor is non-ideal due to slotting, variations in airgap, magnetic saturation etc. a group of unwanted flux density harmonics B_{sh} are generated in addition to the fundamental component (Heller & Hamata, 1977):

$$B_{sh} = \sum_i k_{sh,i} U e^{j(w_i \varphi - \omega_i t + \beta_i)} \tag{12}$$

, where w_i is wave number. These flux density harmonics are also known as space harmonics; they are inherent for the given motor design and exist always, even with pure sinusoidal supply voltage. Once the motor is fed with frequency converter, the voltage harmonics due to non-sinusoidal supply generate an additional, unwanted group of flux density harmonics B_{th}:

$$B_{th} = \sum_l k_{th,l} U_{th,l} e^{j(w_l \varphi - \omega_l t + \gamma_l)} \tag{13}$$

, where $U_{th,l}$ is the amplitude of the supply voltage time harmonic component l. These flux density harmonics are also known as time harmonics; they are dependent of the spectral components of the converter voltage supply. As a result, the total magnetic flux density B_{Tot} becomes:

$$B_{Tot} = B_1 + B_{sh} + B_{th} \tag{14}$$

The interaction with two flux density waves generates a magnetic traction (or pressure) acting on the stator tooth tip. The formulation used here is based on Maxwell stress tensor, which gives for radial- $\tau_{r,i,l}$ and circumferential traction $\tau_{\varphi,i,l}$:

$$\tau_{r,i,l} \approx \frac{1}{2\mu_0}\left(B_{Tot,r,i,l} - B_{Tot,\varphi,i,l}\right)^2 \approx$$

$$\frac{1}{2\mu_0}\Big(B_{1r}\left(B_{sh,i,r} + B_{th,l,r}\right) - 2B_{1r}B_{1\varphi}\left(B_{sh,i,r} + B_{th,l,r}\right)\left(B_{sh,i,\varphi} + B_{th,l,\varphi}\right) + B_{1\varphi}\left(B_{sh,i,\varphi} + B_{th,l,\varphi}\right)\Big) \tag{15}$$

$$\tau_{\varphi,i,l} \approx \frac{1}{\mu_0} B_{Tot,r,i,l} B_{Tot,\varphi,i,l} \approx \frac{1}{\mu_0}\left(B_{1r} + B_{sh,i,r} + B_{th,l,r}\right)\left(B_{1\varphi} + B_{sh,i,\varphi} + B_{th,l,\varphi}\right) \tag{16}$$

, where subscripts r and φ denote radial and circumferential component, respectively and μ_0 is the permeability of vacuo. In the equations above, only the most dominant components are retained i.e., the ones with B_1 as another term in multiplication. The reason for this is that B_1 is by far the largest component in the flux density wave group. Finally, the total radial- and circumferential traction waves can be presented as:

$$\tau_r = \sum_n \tau_{r,n} e^{j(w_n \varphi - \omega_n t + \delta_n)} \text{ and } \tau_\varphi = \sum_m \tau_{\varphi,m} e^{j(w_m \varphi - \omega_m t + \delta_m)} \tag{17}$$

Figure 6 shows an example of a radial traction wave for wavenumbers 2 and 6.

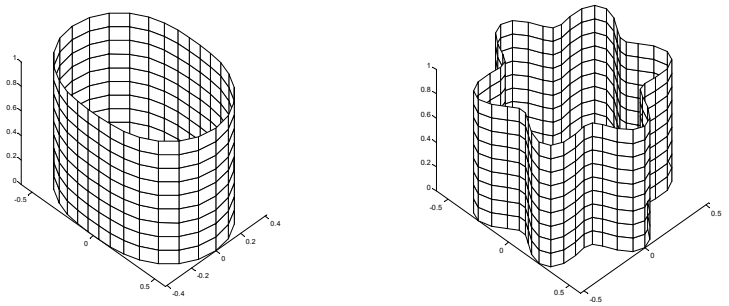

Figure 6: Radial force/traction waves: Left: w = 2, Right: w = 6

3.2. Voltage supply types

Majority of the electric motors used in the world are three phase motors either in star or delta connection, which is also the case with large share of the electric propulsors. However, there exists a group of motors with special winding arrangements such as N-phase, double windings etc., which are not dealt here.

3.2.1. Sinusoidal a.k.a. Direct-on-line or DOL

The most common supply type still used to energize electric motors is sinusoidal supply i.e., the motor is connected to standard electric grid with either 50 or 60 Hz. A motor with sinusoidal supply generates only the fundamental- and space harmonic flux densities $B_{Tot} = B_1 + B_{sh}$. An electric motor with sinusoidal voltage supply generates the minimum achievable sound level for that motor design, which is called self-noise. Figure 7 shows a sinusoidal line-to-line (L2L) voltage time history and spectrum.

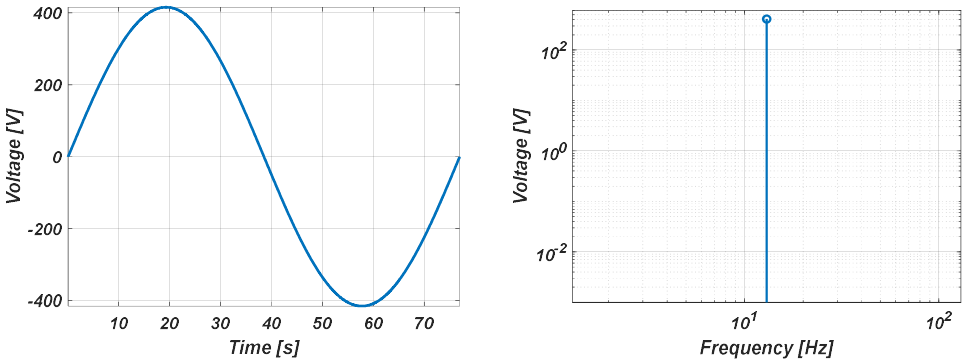

Figure 7: Sinusoidal L2L voltage. Left: Time history, right: Spectrum

*3.2.2. Frequency converter a.k.a. Variable Speed/Frequency Drive or VSD/VFD – **Topologies***

An electric motor supplied with sinusoidal voltage supply lacks the speed and torque control, since the supply frequency is fixed by the electric grid. For this reason, the industry developed a speed control principle based on semiconductors roughly 50 years ago. In the principle the fundamental voltage is built up by short rectangular pulses with varying duration and polarity, which results in device called frequency converter. The two most important properties affecting MURN are the topology and control principle of the converter used. The topology of the converter describes how the semiconductor switches chopping the DC-link voltage are connected to form a motor input voltage. One important topology feature is the number of DC-levels available for chopping. Figure 8 shows the motor terminal Line-to-Line (L2L) voltage of two and seven level converters, respectively.

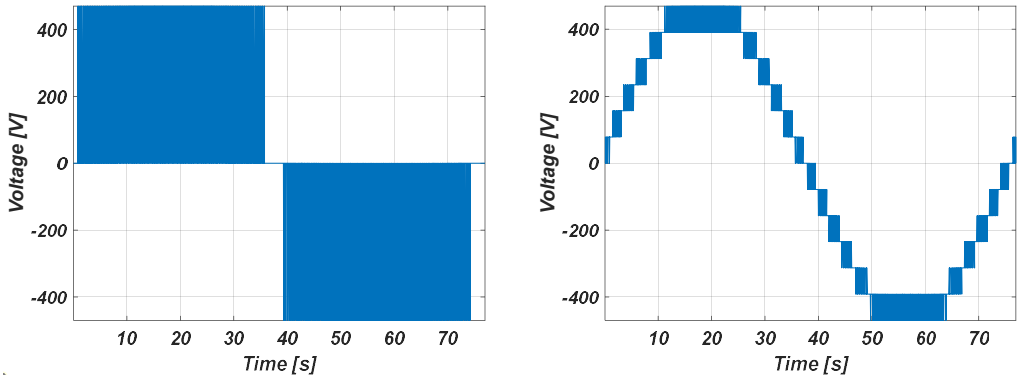

Figure 8: Frequency converter L2L output voltage. Left: 2-level, right: 7-level

*3.2.3. Frequency converter – **Control Principles***

A motor with frequency converter supply generates the fundamental-, space- and time harmonic flux densities:

$$B_{Tot} = B_1 + B_{sh} + B_{th} \tag{18}$$

The used control principle has a strong influence on B_{th}. Basically all the control principles are based in some form on Pulse-width modulation (PWM, see Pulse-width modulation - Wikipedia). The most common control methods are:

1. Fixed carrier PWM, where the carrier wave is sawtooth wave with constant fundamental frequency.
2. Pseudo PWM, which is some adaptation of the former.
3. Random PWM, where the carrier frequency is slightly varying.
4. Direct torque control (DTC), which is based on keeping the flux and torque trajectories within a certain error bound. The bound limits are also known as hysteresis limits. In this control scheme f_c is not constant nor set by the user but is merely an outcome of the applied hysteresis settings → tighter limits → higher average f_c.
5. Model predictive pulse pattern control (MP^{3}C or MP3C), which uses optimized pulse patterns (OPP) to reduce current harmonics or noise (Geyer et. al, 2012).

The focus will be on Pseudo PWM and DTC from here on. Figure 9 shows the motor terminal L2L voltage spectra of Pseudo PWM and DTC converters, respectively.

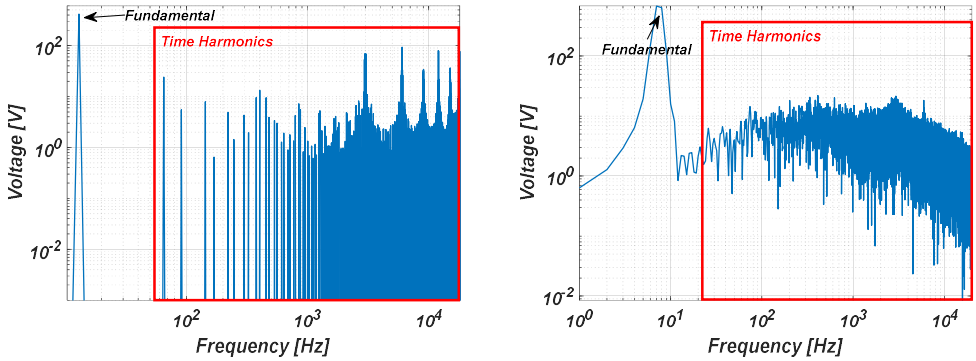

Figure 9: Frequency converter L2L output voltage spectra. Left: Pseudo PWM, right: DTC

3.3. MURN modelling procedure

The method used to compute MURN for a given voltage waveform is based on the concept of unit wave responses (Roivainen, 2009). Sound power unit-wave response for magnetic traction wave w expresses how much sound power a traction wave with amplitude of 1 Pa with wavenumber w generates for a given motor structure. The MURN response for given voltage waveforms is evaluated by weighing the unit-wave responses with the computed magnetic tractions.

3.3.1. Simplified approach

The simplified approach assumes that there is no coupling or feedback between magnetic traction, structural deformations and sound radiation. The MURN modelling procedure is shown in Figure 10. The motivation for using simplified method comes from the fact that it needs a way less computation memory & time compared to coupled approach.

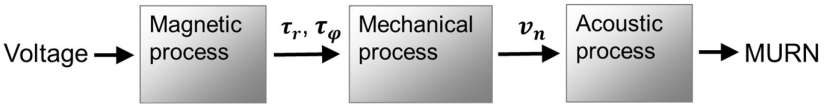

Figure 10: Simplified MURN modelling procedure

The magnetic process involves solving a magnetic field equation using a 2- or 3D FE-method. The post-processing is then carried out to map tractions τ_r and τ_φ from cartesian time-space domain to cylindrical frequency-wavenumber domain using 2D FFT.

The obtained tractions are used as a boundary load for the structural dynamic FE-model, the deflections of which are then evaluated by modal superposition or direct solution in-vacuo.

The sound radiation task needs structure-water surface normal velocities v_n as a boundary condition for exterior radiation problem. In the simplified approach an approximation of Kirchhoff-Helmholtz formulation such as High-Frequency Boundary Element Method (HFBEM) is used (Herrin et. al, 2003) to estimate the radiated sound power W_0. The corresponding (monopole) source level L_{s0} is:

$$L_{s0} = 10 \lg \left[\frac{W_0 \rho_f c_f}{4\pi p_{ref}^2} \right] \tag{19}$$

, where ρ_f is the water density, c_f speed of sound in water and $p_{ref} = 1$ µPa is the reference pressure.

3.3.2. *Coupled approach*

The coupled approach assumes a coupling between structural deformations and sound radiation. The MURN modelling procedure is shown in Figure 11.

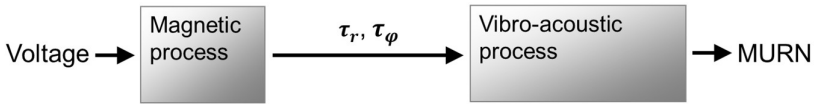

Figure 11: Coupled MURN modelling procedure

The obtained tractions are used as a boundary load for the structural dynamic FE-model, the deflections of which are then evaluated by direct solution in water. The sound radiation equations (fluid loading) are now included in the structural mechanics solver already and the estimate of the radiated sound power W_c is directly available. The corresponding (monopole) source level L_{sc} is:

$$L_{sc} = 10 \lg \left[\frac{W_c \rho_f c_f}{4\pi p_{ref}^2} \right] \tag{20}$$

3.3.3. *Discussion*

As an example, both methods were used to compute the MURN source-level for generic electric podded propulsor with LV frequency converter using Pseudo PWM modulation and 3 kHz carrier frequency. The comparison of the results is shown in Figure 12. As expected, the simplified method (black) overestimates the source level remarkably if fluid loading is neglected.

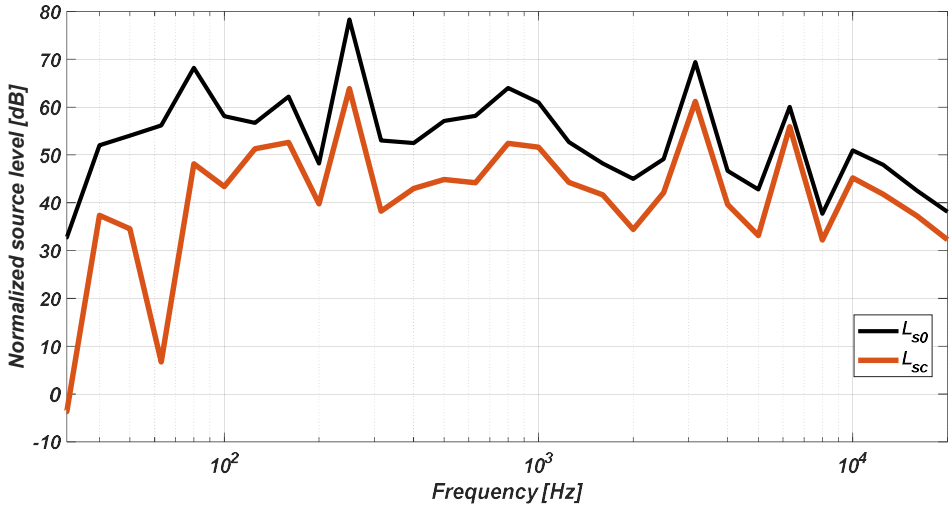

Figure 12: Simplified- vs. Coupled MURN modelling results

3.4. MURN mitigation

MURN mitigation includes all the measures needed to reduce converter and/or self-noise of the propulsor. The self-noise mitigation usually consists of an improved motor design such as optimized slot-numbers, modified stator winding designs, modified pole shaping or active systems for reduced torque ripple. In the following the most typical methods for MURN mitigation are presented and described.

3.4.1. Transit conditions (>= 80 % of nominal propulsion power)

- Modification of switching frequency (Fixed carrier or Pseudo PWM) or hysteresis optimization (DTC).
- Converter topology (N-level) sets the baseline for MURN, see Figure 13.
- Sine filter is the most classical solution for reduction of MURN.

3.4.2. Cruise or Research conditions (<= 20 % nominal propulsion power)

In addition to the options available for Transit conditions, the following additional methods are available for lower power operations:

- The converter output voltage is directly proportional to the shaft speed and thus the supply frequency of the propulsor. Thus, the DC-link voltage can be reduced as there is no need for full voltage due to low speed, which helps to reduce the time harmonic flux density components B_{th}.
- Main flux reduction (a.k.a. field weakening) is especially effective for synchronous motors with external excitation. This lowers the fundamental flux density B_1.

Figure 13 shows some examples of MURN mitigation. The left graph considers MURN mitigation of MV-drive with DTC-control, whereas the right concentrates on LV-drive with Pseudo PWM-control with f_c=3000 Hz.

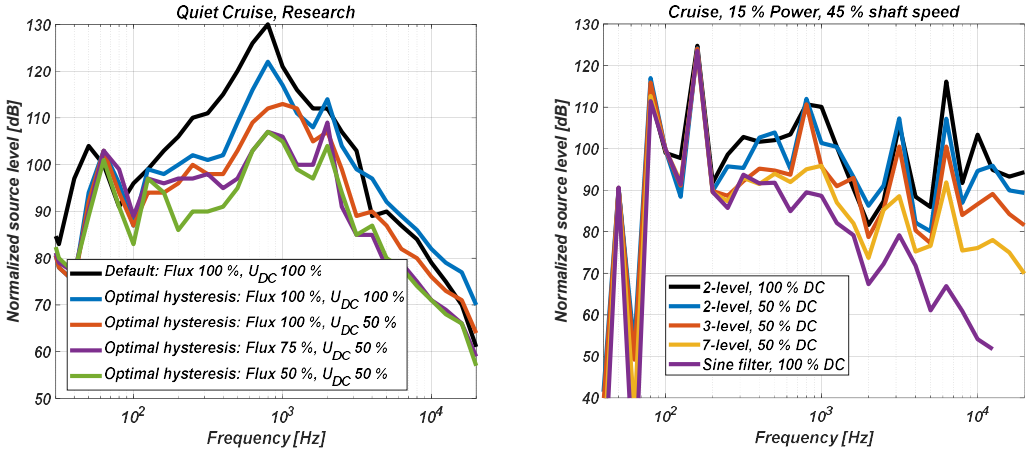

Figure 13: MURN mitigation at cruise/research conditions. Left: MV-drive, right: LV-drive.

4. Onboard measurement systems – CLUE

URN is normally measured only once during a sea trial in far-field using stationary hydrophones with a distance to the ship for two fixed operating conditions, typically 11 knots and 80% MCR (ISO, 2016), which causes URN emissions during off-design conditions to stay largely unknown. This fact has led to introduction of various on-board URN-measurement methods such as DNV's simplified method (near-field method) using pressure sensors mounted through the hull (DNV, 2022). Obviously, on-board methods increase flexibility, are cost-effective and enable continuous monitoring of PURN. However, podded vessels have a larger range of characteristics (MURN), which currently are not well captured by the existing near-field methods.

CLUE (Continuous Logging of Underwater noise Emissions) was a development study and a prototype design of measurement system for URN, which was built and tested in-situ with a vessel using Azipod® propulsion (duration 2 years – started 1.4.2022). The project members were ABB, DNV and Transport Canada. The final report can be downloaded from ClearSeas.org (ClearSeas, 2024). To study the added URN emissions due to motor electromagnetics, the existing DNV's near-field method was augmented by vibration measurements from the motor inside the podded propulsor. CLUE system overview is shown in Figure 14 and an example of calibration

results in Figure 15. From the figure it can be clearly seen that the current near-field method needs to be augmented with some form of additional sensing for podded propulsors.

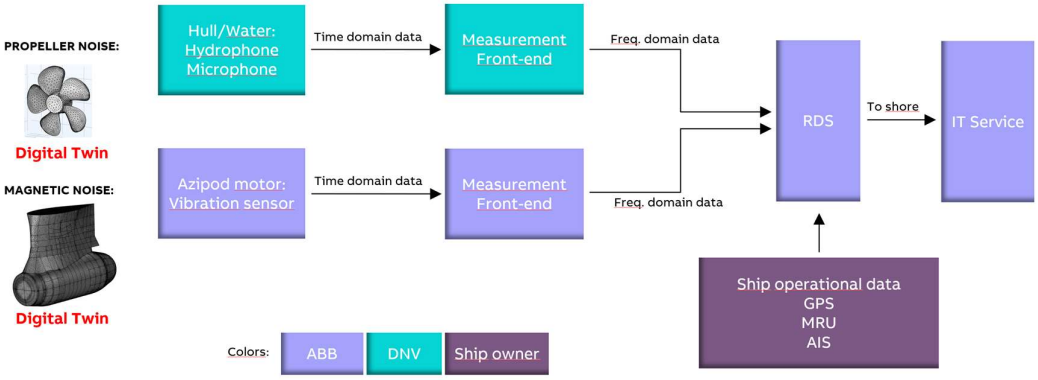

Figure 14: CLUE system description.

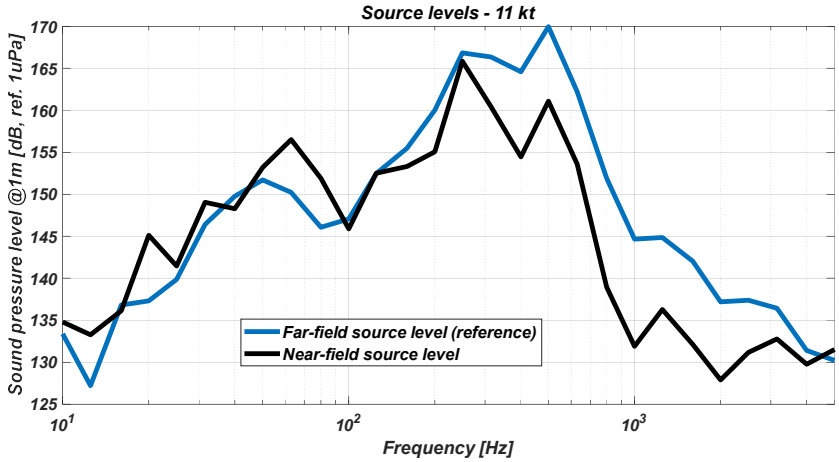

Figure 15: CLUE system calibration results (Near-field vs. Far-field results)

5. Conclusions

This article discusses the main phenomena causing URN emissions from Azipod® propulsor, namely the propeller emitted- and electromagnetic noise (PURN & MURN). At first, the most important noise generation mechanisms for each noise source are presented and discussed. Then, sound radiation modelling methods are addressed in general level for simplicity, followed by description of various mitigation measures. Finally, a novel on-board measurement system for Azipod® propulsors is introduced.

References

Bosschers J., 2018. "Propeller Tip-Vortex Cavitation and its Broadband Noise", PhD thesis, University of Twente.

Burgers J., 1948. "A Mathematical Model Illustrating the Theory of Turbulence", *Advances in Applied Mechanics*, **1**, 171–199.

ClearSeas, 2024, https://clearseas.org/wp-content/uploads/TN24-10-CLUE-Final-Report.pdf

DNV-CG-0313. Edition July 2022, "Measurement procedures for noise emission".

Franc F.-P., Michel J.-M., 2004. "Fundamentals of Cavitation", Springer. 264 p. ISBN 0-4020-2233-8.

T. Geyer, et al., 2012. "Model Predictive Pulse Pattern Control", IEEE Trans. on Industry Applications, vol. 48, no 2, March/April 2012, pp. 663–676

Heller B. & Hamata V., 1977. “Harmonic Field Effects in Induction Machines”, Elsevier.

Herrin, D., Martinus, F., Wu, T., and Seybert, A., 2003. "A New Look at the High Frequency Boundary Element and Rayleigh Integral Approximations," SAE Technical Paper 2003-01-1451.

ISO 17208-1: 2016, “Underwater acoustics — Quantities and procedures for description and measurement of underwater sound from ships — Part 1: Requirements for precision measurements in deep water used for comparison purposes”.

Plesset, M., 1949. “The dynamics of cavitation bubbles”, Journal of Applied Mechanics, 16, 277–282.

Rankine, W., 1869. “A Manual of Applied Mechanics”, 5th Edition, revised. Charles Griffin and Company, Stationers’ Hall Court.

Roivainen, J., 2009. “Unit-Wave Response-Based Modeling of Electromechanical Noise and Vibration of Electrical Machines”, Doctoral Dissertation. Helsinki University of Technology, 186 pages. ISBN: 978-951-22-9910-2.

Timar P. L., 1989. “Noise and Vibration of Electrical Machines”, Elsevier, 1989.